Dynamic morphoskeletons in development

Mattia Serra[a], Sebastian Streichan[b,c], Manli Chuai[d], Cornelis J. Weijer[d], and L. Mahadevan[a,e,f,g,1]

[a]School of Engineering and Applied Sciences, Harvard University, Cambridge, MA 02138; [b]Kavli Institute of Theoretical Physics, University of California, Santa Barbara, CA 93106; [c]Department of Physics, University of California, Santa Barbara, CA 93106; [d]Division of Cell and Developmental Biology, School of Life Sciences, College of Life Sciences, University of Dundee, Dundee DD1 5EH, United Kingdom; [e]Department of Organismic and Evolutionary Biology, Harvard University, Cambridge, MA 02138; [f]Department of Physics, Harvard University, Cambridge, MA 02138; and [g]Kavli Institute for NanoBio Science and Technology, Harvard University, Cambridge, MA 02138

Edited by Eric D. Siggia, The Rockefeller University, New York, NY, and approved March 19, 2020 (received for review May 27, 2019)

Morphogenetic flows in developmental biology are characterized by the coordinated motion of thousands of cells that organize into tissues, naturally raising the question of how this collective organization arises. Using only the kinematics of tissue deformation, which naturally integrates local and global mechanisms along cell paths, we identify the dynamic morphoskeletons behind morphogenesis, i.e., the evolving centerpieces of multicellular trajectory patterns. These features are model- and parameter-free, frame-invariant, and robust to measurement errors and can be computed from unfiltered cell-velocity data. We reveal the spatial attractors and repellers of the embryo by quantifying its Lagrangian deformation, information that is inaccessible to simple trajectory inspection or Eulerian methods that are local and typically frame-dependent. Computing these dynamic morphoskeletons in wild-type and mutant chick and fly embryos, we find that they capture the early footprint of known morphogenetic features, reveal new ones, and quantitatively distinguish between different phenotypes.

morphogenesis | cell motion | coherent structures | finite time Lyapunov exponent

During embryonic development, cells undergo large-scale coordinated motion during the process of tissue and organ formation that together shape the embryo. Understanding these processes requires integrating molecular, cellular, and multicellular perspectives across a range of length and time scales, linking cellular-level gene expressions and regulatory signaling networks (1–4) to long-range intercellular interactions and mechanical force generation (5–8). These approaches are complemented by advances in live imaging techniques (9) that allow for the detailed tracking of cellular trajectories (10–14), providing exquisite geometric and kinematic information on tissue morphogenesis. Some natural questions that these experimental approaches raise include: Can one correlate cell position, cell velocity, and cell–cell interactions with cell- and tissue-fate decisions? Can one link gene-expression levels and cellular trajectories with active force generation to help unravel the biophysical basis for morphogenesis? Can one quantitatively analyze cell-motion data to predict the ultimate outcomes of tissue morphogenesis and organ development in normal and pathological situations? Here, we address the last question by providing a mathematically grounded framework to determine the evolving centerpieces of morphogenetic movements using experimentally determined cellular trajectories, thus providing an important step in bridging the gap between bottom-up mechanistic approaches and top-down statistical and computational approaches (15, 16) (Fig. 1*A*).

Minimally, any framework that aims to analyze spatiotemporal trajectories in morphogenesis requires a self-consistent description of cell motion that is independent of the choice of reference frame or parametrization. This frame-invariant description of cell patterns is termed objective (17) and ensures that the material response of a deforming continuum, e.g., biological tissue, is independent of the observer. To quantify this notion, we start by considering two coordinate systems used to describe cell flows: the first corresponding to $\mathbf{x}\in\mathbb{R}^3$ and a second one, $\bar{\mathbf{x}}$, defined as $\bar{\mathbf{x}}(t)=\mathbf{Q}(t)\mathbf{x}(t)+\mathbf{b}(t)$, where $\mathbf{Q}(t),\mathbf{b}(t)$ are a time-dependent rotation matrix and translation vector. A quantity is objective (frame invariant) if the corresponding descriptions in the $\mathbf{x}$ and $\bar{\mathbf{x}}$ transform according to specific rules (17). In particular, scalars must remain the same $\bar{c}=c$, vectors must transform as $\mathbf{x}$, and second-order tensors as $\bar{\mathbf{A}}=\mathbf{QAQ}^{\top}$. Taking the time derivative of $\bar{\mathbf{x}}$, $\dot{\bar{\mathbf{x}}}(t)=\dot{\mathbf{Q}}(t)\mathbf{x}(t)+\mathbf{Q}(t)\dot{\mathbf{x}}(t)+\dot{\mathbf{b}}(t)$, one can easily see that the velocity field and the streamlines, which are trajectories of the frozen velocity field, are frame-dependent, i.e., any metrics based on them for comparative purposes are likely to be erroneous (Fig. 1*B*), owing to the inability to remove the dependence on artifacts associated with variations in the choice of reference frames, etc.

Driven by the recent revolution in imaging morphogenetic flows and cellular movements (18, 19), a range of approaches have been developed to characterize mesoscopic cellular behavior. These include statistical tools based on the connectivity between neighboring sites (20) and methods quantifying cell-shape changes and cell intercalation by mapping the temporal evolution of strain rates between neighboring cells (5, 6). However, because of the general time dependence of cell motion, any velocity or velocity-gradient features such as streamlines or strain rates differ substantially from Lagrangian trajectory patterns that integrate over the history of particles motion.

As an illustrative example, consider the analytic velocity field $\mathbf{v}(\mathbf{x},t)=(x_1\sin 4t+x_2(2+\cos 4t)+0.2x_1x_2)\mathbf{e_1}+(x_1(\cos 4t-2)-x_2\sin 4t+0.3x_1x_2)\mathbf{e_2}$, whose objective rate of strain

Significance

Coordinated cell migration is a hallmark of tissue morphogenesis during development and emerges from the combination of local cell behaviors and distributed chemo-mechanical interactions integrated across many spatial and temporal scales. A challenge in the field is to predict developmental outcomes of tissue morphogenesis using cellular trajectories. We provide a rigorous kinematic framework to analyze cell motion and identify robust multicellular attractors and repellers in space and time. Our results yield a scheme for comparing different morphogenetic phenotypes and help bridge the gap between bottom-up and top-down modeling approaches to morphogenesis.

Author contributions: M.S. and L.M. designed research; M.S. performed research; M.S., S.S., M.C., C.J.W., and L.M. contributed new reagents/analytic tools; M.S., S.S., C.J.W., and L.M. analyzed data; and M.S. and L.M. wrote the paper.

The authors declare no competing interest.

This article is a PNAS Direct Submission.

Published under the PNAS license.

Data deposition: The data used in this paper are available to individual researchers on request from the corresponding author.

[1]To whom correspondence may be addressed. Email: lmahadev@g.harvard.edu.

This article contains supporting information online at https://www.pnas.org/lookup/suppl/doi:10.1073/pnas.1908803117/-/DCSupplemental.

First published May 7, 2020.

Downloaded at Harvard Library on June 14, 2020

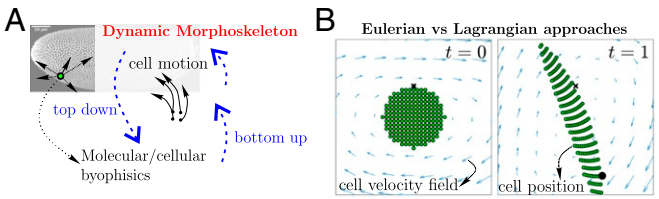


Fig. 1. (*A*) Sketch of bottom-up and top-down approaches to study cell motion. Bottom-up approaches study local mechanisms driving cells. Top-down approaches study patterns of cell motion caused by local and global driving mechanisms. The DM uncovers the centerpieces of cell-trajectory patterns in space and time. (*B*) Snapshots of a simple analytic velocity field (blue) and its Lagrangian particle positions (green). The black dot marks the position of a particle started from the black x marker at time 0. The complete time evolution is available as Movie S1.

tensor $\mathbf{S}(\mathbf{x},t)$ has components $S_{ij}=(\partial v_i/\partial x_j+\partial v_j/\partial x_i)/2$. Fig. 1*B* shows that the frame-dependent velocity field (blue) suggests a vortex-type structure, while Lagrangian particles (green) correctly reveal the presence of exponentially stretching deformations. Even if one averages the objective dominant rate of strain eigenvalue at a fixed (Eulerian) location marked by the black x over a time interval $[0,1]$, this average completely ignores the Lagrangian positions (black dot) explored by a trajectory starting from the x marker at time 0. Using explicit formulas relating Eulerian and Lagrangian deformations, in *SI Appendix*, we show that local changes of tissue flows can lead to global effects, which are detectable only by a Lagrangian analysis. This simple example and observations show that Eulerian methods, regardless of their objectivity, are inherently suboptimal for studying cellular flows and suggest that a frame-invariant Lagrangian method is more suitable to assess global flows such as those seen in morphogenesis.

Here, we use the notion Lagrangian Coherent Structures (LCSs) (21), initially derived to study fluid flow patterns, to create an objective kinematic framework for analyzing cell motion. This allows us to uncover the dynamic morphoskeletons (DMs) underlying morphogenesis, which quantify Lagrangian tissue deformations and correspond to the attracting and repelling organizers of cell trajectories in space and time. We illustrate our results on wild-type (WT) and mutant embryo imaging datasets obtained by light-sheet microscopy (LSM) in the context of primitive streak (PS) formation in the chick and early gastrulation in the fly.

Defining the DM Using LCSs

In general, trajectories of time-dependent dynamical systems have complicated shapes, are sensitive to changes in their initial conditions, and are characterized by multiple spatial and temporal scales. However, underlying these complicated paths, one often finds a robust skeleton that organizes the spatiotemporal structures in the dynamical system—referred to as LCSs (21)—which shapes trajectory patterns and provides a simplified description of the overall dynamics. They involve information obtained by integrating the trajectories in space–time and, thus, serve as a memory trace of the dynamical system. They can be defined for large or small time spans (22). In a general setting, we schematize this in Fig. 2 and illustrate the impact of attracting and repelling LCSs on trajectory patterns over a time interval $[t_0,t]$. The combined effect of attracting and repelling LCSs is shown in Fig. 2*B*. For example, blue trajectories represent two cells that were initially very close (blue dots), but end up far apart. Even though they end up far apart, and, hence, are apparently subject to very different fates, they end up on the same attracting LCS after separating from a repelling LCS. Therefore, assessing the system through individual trajectories, despite being Lagrangian, will return poor results.

While there are a number of methods to determine Lagrangian (i.e., with memory) coherent structures (23), the finite time Lyapunov exponent (FTLE), despite its limitations (21), remains the most used because it is computationally simple. The FTLE is characterized by a scalar field used to locate regions of high separation (or convergence) of initially close (distant) particles over $[t_0,t]$. Denoting by $\mathbf{v}(\mathbf{x},t)$ a velocity field obtained from imaging data, the induced Lagrangian flow map $\mathbf{F}_{t_0}^{t}(\mathbf{x}_0)$ is given by

$$\mathbf{F}_{t_0}^{t}(\mathbf{x}_0)=\mathbf{x}_0+\int_{t_0}^{t}\mathbf{v}(\mathbf{F}_{t_0}^{\tau}(\mathbf{x}_0),\tau)\,d\tau, \qquad [1]$$

which maps the initial positions (of cells, membranes, or nuclei, for example) $\mathbf{x}_0$ at time t_0 to their final positions at time t. The FTLE is then defined as

$$FTLE_{t_0}^{t}(\mathbf{x}_0)=\frac{1}{|T|}\ln\left(\max_{\delta\mathbf{x}_0}\frac{|\overbrace{\nabla\mathbf{F}_{t_0}^{t}(\mathbf{x}_0)\delta\mathbf{x}_0}^{\delta\mathbf{x}_t}|}{|\delta\mathbf{x}_0|}\right), \qquad [2]$$

where $|\cdot|$ represents the absolute value and ∇ the Jacobian with respect to $\mathbf{x}_0$. The FTLE is thus a measure of the maximum separation rate between a trajectory starting at $\mathbf{x}_0$ and a neighboring one starting at $\mathbf{x}_0+\delta\mathbf{x}_0$, over $[t_0,t]$ (Fig. 2*A*) (see *SI Appendix* for explicit formulas for computing Eq. **2**).

We note that the FTLE depends on the base time t_0, the spatial location $\mathbf{x}_0$—which correspond to the positions of Lagrangian particles at the base time—and the final time t, which

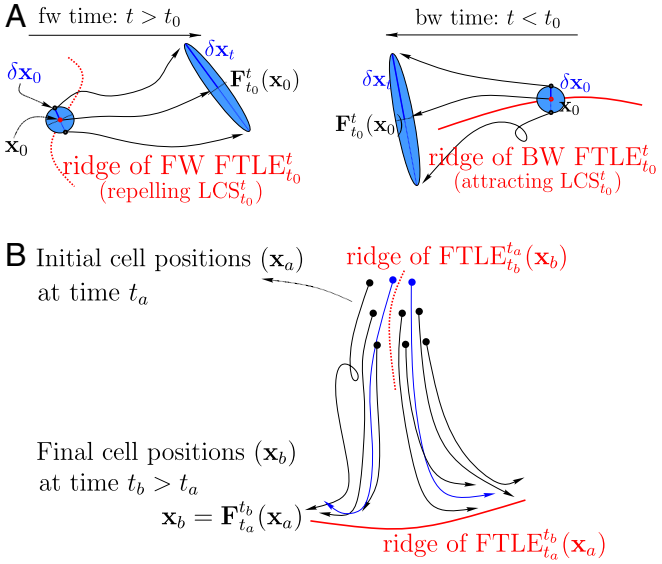


Fig. 2. (*A*) The $FTLE_{t_0}^{t}(\mathbf{x}_0)$ measures the maximum separation ($\sim|\delta\mathbf{x}_t|/|\delta\mathbf{x}_0|$) induced by the flow at $\mathbf{x}_0$ over the time interval $[t_0,t]$ between two initially close points in the neighborhood of $\mathbf{x}_0$. A forward-time FTLE ridge—a set of points with high FTLE values—marks a repelling LCS whose nearby points from opposite sides of the ridge will experience the maximum separation over $[t_0,t]$, $t>t_0$. Similarly, a backward-time FTLE ridge demarcates an attracting LCS, i.e., a distinguished curve at t_0 which has attracted initially distant particles over $[t,t_0]$, $t<t_0$. (*B*) Illustration of attracting and repelling LCSs over a time interval of interest $[t_a,t_b]$, $t_b>t_a$, during which cells move from their initial configuration $\mathbf{x}_a$ to their final one $\mathbf{x}_b=\mathbf{F}_{t_0}^{t}(\mathbf{x}_a)$. The forward FTLE is a scalar field over $\mathbf{x}_a$, while the backward FTLE is over $\mathbf{x}_b$. Blue trajectories show cells that start close to each other from opposite sides of a repelling LCS and end up far apart along the same attracting LCS.

Downloaded at Harvard Library on June 14, 2020

sets the time scale $T = t - t_0$. As illustrated in Fig. 2*A*, a set of points $\mathbf{x}_0$ with high forward FTLE values (FW FTLE ridge) marks a region at t_0, whose neighboring particles from opposite sides of the ridge will get repelled, achieving maximum separation at the later time $t = t_0 + T,\ T > 0$. Similarly, a backward FTLE (BW FTLE) ridge marks regions that at the base time t_0 have attracted initially distant particles over the time interval $[t_0 + T, t_0],\ T < 0$. Together, the FW and BW FTLE fields associated with varying time scales T uncover the exact spatial locations of repelling and attracting LCSs, along with the times at which they appear and cease to exist. We further note that, over a time interval of interest $[t_a, t_b],\ t_b > t_a$, during which cells move from their initial configuration $\mathbf{x}_a$ to their final one $\mathbf{x}_b = \mathbf{F}_{t_a}^{t_b}(\mathbf{x}_a)$, the FW FTLE is a scalar field over $\mathbf{x}_a$, while the BW FTLE is a scalar field over $\mathbf{x}_b$. Therefore, over $[t_a, t_b]$, trajectories initially at opposite sides of FW FTLE ridges will be repelled from each other and get attracted to BW FTLE ridges by time t_b (Fig. 2*B*).

A mechanical interpretation of Eq. **2** follows by noting that the $\mathrm{FTLE}_{t_0}^{t}(\mathbf{x}_0)$ is proportional to the logarithm of the highest eigenvalue $\lambda_2(\mathbf{x}_0)$ of the Cauchy–Green strain tensor $\mathbf{C}_{t_0}^{t}(\mathbf{x}_0) = [\nabla \mathbf{F}_{t_0}^{t}(\mathbf{x}_0)]^{*} \nabla \mathbf{F}_{t_0}^{t}(\mathbf{x}_0)$ (17), a naturally invariant measure of deformation of a continuous medium. Hence, it represents the maximum deformation induced by the flow over $[t_0, t]$ on an infinitesimal area element centered at $\mathbf{x}_0$ (Fig. 2*A*) and, thus, provides an exact link between the DM and the Lagrangian strain experienced by cells during morphogenesis. Separation or convergence of cell trajectories captured by the FTLE can arise from a combination of isotropic (volume or area) changes—due, e.g., to cell divisions, ingression, and area change—and anisotropic (shear) deformations—due to cell-shape changes and cell intercalation. To quantify these two effects, we define the percentage of Lagrangian attraction due to anisotropic deformations over $[t, t_0], t < t_0$ as

$$A_{t_0}^{t} = \frac{\sqrt{\lambda_2} - \sqrt[4]{\det \mathbf{C}_{t_0}^{t}}}{|\sqrt[4]{\det \mathbf{C}_{t_0}^{t}} - 1| + \sqrt{\lambda_2} - \sqrt[4]{\det \mathbf{C}_{t_0}^{t}}}\%, \qquad [3]$$

where we dropped the $\mathbf{x}_0$ dependences (*SI Appendix*, *Methods*). The same formula in forward time ($t > t_0$) quantifies the percentage of anisotropic repulsion. Therefore, Eqs. **2** and **3** completely quantify and characterize tissue deformations. We now deploy these concepts on two paradigmatic problems in large-scale morphogenetic flows: PS formation in the chicken embryo and gastrulation in the whole fly embryo. In both cases, we will follow the spatiotemporal evolution of the DM in terms of the FTLE fields as a function of their memory T and, thus, determine the attracting and repelling manifolds underlying tissue organization. We also compare the DM and the overall Lagrangian deformations in WT and mutant phenotypes.

Results

PS Formation in Chicken Embryo. The PS is a hallmark of bilateral symmetry in many organisms, is the site of ingression of the mesoderm and endoderm precursors, and involves large-scale cell flows to form an axial structure that serves to organize embryogenesis. The formation of this structure is best understood in the chicken embryo and involves coordinated flow of more than 100,000 cells in the epiblast. Here, we generate a cell-velocity dataset of an embryo with Green Fluorescent Protein labeled cell membranes (Myr-GFP) using a dedicated LMS, as described in ref. 24. The velocity field is defined on a uniform rectangular grid of size 4.77 × 3.14 mm over a time interval of approximately 12 h from the freshly laid egg [Eyal-Giladi and Kochav stage XII (EGK-XII)] (25) to Hamburger Hamilton Stages 4 (HH4) (26), prior to the onset of tissue movement, with spatial resolutions of $0.65\mu m$ and temporal resolution of 3 min. As in ref. 24, we filtered the cell velocities using a centered averaging filter with a 5×5 spatial and a $5-$time instances temporal window sizes. Movie S2 shows the velocity field overlaid over the experimental fluorescence images of the epiblast surface. We then computed attracting and repelling LCSs as BW and FW FTLE (*SI Appendix*, *Methods*) for a set of time scales $|T|$ spaced by 20 min.

Fig. 3 *A*, *Left* shows the FW FTLE_{0}^{12h}, indicating the presence of two repellers. The first repeller demarcates the boundary between the embryonic and extraembryonic area. The second repeller, in contrast, demarcates a sharp boundary within the embryonic region. Fig. 3 *A*, *Right* shows the BW FTLE_{12h}^{0}, highlighting the presence of an attractor that corresponds to the formed PS. Passively transporting with $\mathbf{F}_{12h}^{0}$ the BW FTLE field, which is based at the final (12 h) cell configuration to the initial time (0 h), we identify the initial set of the mesendoderm precursor cells (yellow region bounded by the black level set in Fig. 3 *A*, *Center*) that will finally form the PS. We overlay repeller two on this plot, and, marking cells on its different sides in magenta and green, we show that it sharply divides the A and P parts of the PS, as confirmed by the final cell positions. From Movie S3, which shows a sequence of Fig. 3*A* for different $|T|$, we observe that repeller two forms around T = 400 min.

It is well established that cells in the anterior and posterior streak differentially express key genes code for important signals and signal modulators and that cells in various parts of the streak have different fates (27–29). Several of these genes are initially expressed in sickle-shaped regions in the early streak-stage embryo; however, their expression domains separate during the streak extension (*SI Appendix*, Fig. S4). This suggests that repeller two is a dynamic structure associated with the separation of gene-expression domains and a functional readout of cell fate during streak formation, the mechanistic basis for which needs to be investigated in future experiments. For comparison, Movie S3 also shows the averaged velocity field, the evolution of a dense set of points, and the deformation of an initially uniform grid that moves with the flow. Remarkably, repellers remain entirely hidden to these tools. The attractor, instead, cannot be detected by the average velocity diagnostic and becomes visible to the dense set of points and the deforming gird when the PS is already formed. Although the latter two diagnostic are Lagrangian, they do not use the deformation gradient $\nabla \mathbf{F}$, but just the deformation $\mathbf{F}$, hence, requiring longer time compared to the FTLE for identifying attractors. While embryonic regions toward which cells tend to cluster have been studied before (16, 24), our analysis precisely locates in space and time also repelling regions that are key in shaping multicellular patterns and studying cell fate.

Remarkably, already within 60 min, while cells barely moved, the BW FTLE already shows a footprint of the PS forming perpendicularly to the AP direction encircled by a blue ellipse in Fig. 3*B*. Differently from existing studies, where the early location of the PS is obtained by following backward in time the cells belonging to the formed PS (24), our approach does not use future data, hence revealing the footprint of PS formation only from Lagrangian deformations. Fig. 3*C* shows the $A_{t_0}^{t}$ field associated with Fig. 3*B*, highlighting that the Lagrangian attraction giving rise to the early PS footprint is dominated ($\geq 80\%$) by anisotropic deformations. In *SI Appendix*, Fig. S5 and Movie S11, we show a comparison of the BW FTLE, the isotropic Lagrangian convergence, the velocity divergence, and the $A_{t_0}^{t}$. This analysis highlights that the BW FTLE and the $A_{t_0}^{t}$ completely capture and quantify the PS formation and tissue deformations, both of which remain hidden to the Lagrangian and Eulerian isotropic convergence fields.

Downloaded at Harvard Library on June 14, 2020

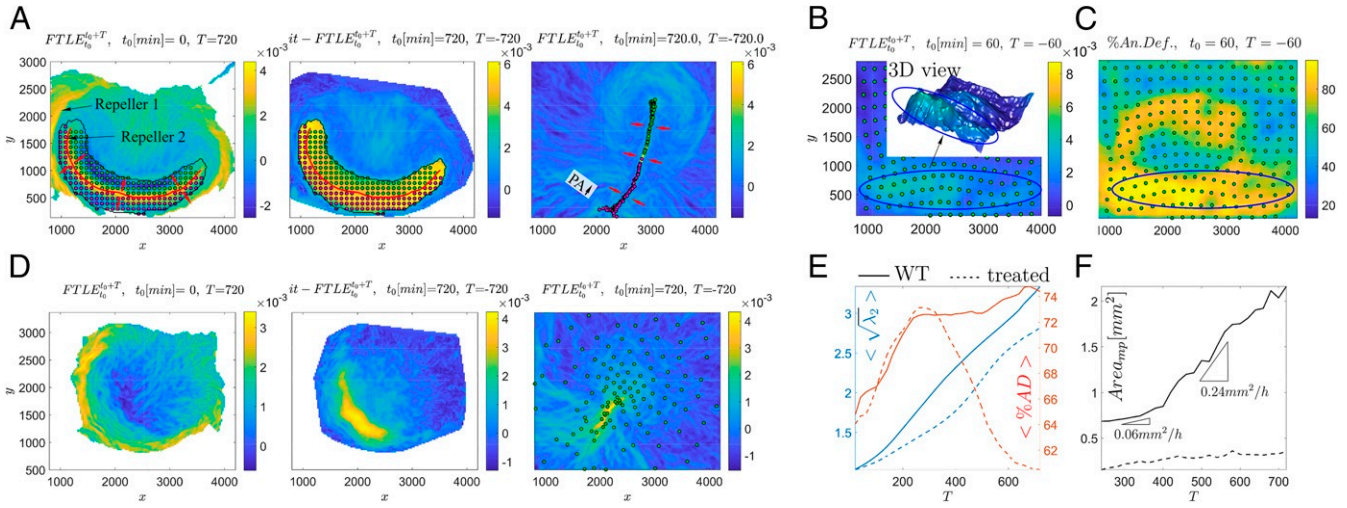


Fig. 3. (*A*, *Left*) FW FTLE corresponding to the full dataset highlights two repelling LCSs. (*A*, *Right*) BW FTLE corresponding to the full dataset highlights the attracting LCS corresponding to the formed PS. (*A*, *Center*) BW FTLE field in *A*, *Right* passively transported by $\mathbf{F}_{12h}^{0}$ to the initial time marks the initial position of the mesendoderm precursor cells, bounded by the solid black line, that will finally form the PS. Cells starting at different sides of repeller two will form the anterior and posterior part of the PS. White areas correspond to the regions where the FTLE is unavailable because trajectories left the domain over which the velocity field is defined. The FTLE has unit min^{-} 1, and the axis units are in micrometers. The time evolution of the FTLE fields and cell positions for different T is available as Movie S3. (*B*) The BW FTLE ridge (attracting LCS) for T = 1 h highlights the early footprint of the PS (blue ellipse) using only data within $[0, 1]h$, during which cells (green dots), initially released on a uniform rectangular grid, barely moved. 3D, three-dimensional. (*C*) The anisotropic deformation field associated with *B* shows that the cell convergence in the early PS formation is dominated $\geq 80\%$ by anisotropic deformations. (*D*) Same as *A* for a chicken embryo treated with an FGF receptor inhibitor. Movie S4 shows the time evolution of the FTLE fields and cell positions for different T. (*E*) Lagrangian tissue deformation quantified as the spatially averaged $\sqrt{\lambda_2}$ (blue), where λ_2 denotes the highest eigenvalue of $\mathbf{C}_0^T(\mathbf{x}_0)$. Red curves show the associated averaged % of anisotropic deformation. (*F*) Quantification of the initial area of the mesendoderm precursor cells that will form the PS (Fig. 3 *A*, *Center*) computed automatically from the FTLE field, as explained in *SI Appendix*, Fig. S6.

Fibroblast growth factor (FGF) signaling is required for the early specification of mesendoderm and early gastrulation movements in the chicken embryo (30, 31). Fig. 3*D* shows the same analysis as Fig. 3*A* for a chicken embryo treated with $1\mu M$ of an FGF receptor inhibitor (LY2874455), which was added at t = 84 min (32). We find that the overall size of the attractor region is smaller compared to the WT, consistent with the FGF treatment. We see that repeller two is absent in the treated embryo, implying that development is inhibited before the functional differentiation of A and P streak cells takes place. Movie S4 shows Fig. 3*D* for different T. As an aggregate measure of Lagrangian tissue deformation, we consider the spatial average of $\sqrt{\lambda_2}$, which measures the ratio of the deformed ellipse major semiaxis to the initial radius of the undeformed infinitesimal circle. Fig. 3*E* shows that after the first $\approx 4h$, the tissue deformation of the WT embryo is $\approx 20\%$ higher compared to the FGF-inhibitor–treated one. By contrast, the average percentage of anisotropic deformation in the two cases is similar in the first $\approx 4h$ and then remains dominant $\geq 72\%$ in the WT, while rapidly decreasing to $\approx 60\%$ in the FGF-treated embryo, indicating a key role for FGF signaling in the maintenance of cell–cell intercalation. While these changes are considerable, further work is required to study their statistics across embryos. In Fig. 3*F*, we quantify the area of mesendoderm precursor cells at the initial time (Fig. 3 *A*, *Center*) that will finally form the PS. We identify the solid black curve delimiting the area automatically from the FTLE field, as described in *SI Appendix*, Fig. S6. The WT embryo area is three times bigger than the treated one before 400 min, which corresponds to the formation of repeller two. After that, the WT area increases at a rate four times higher than before, leading to a final area six times bigger than the FGF-treated embryo.

In *SI Appendix*, Fig. S7, we show the same analysis of Fig. 3*A* using the raw unfiltered velocity. We find that the DM is exceptionally robust to noise and measurement errors and is perfectly computable without ad hoc filtering cell velocities.

Gastrulation in the Fly Embryo. Instead of focusing only on a specific morphogenetic feature, here, we analyze the early development of the entire fly embryo. During gastrulation of *Drosophila*, about 6,000 cells on the embryonic blastoderm on the embryo surface undergo global morphogenetic flow, which induces severe tissue deformation, finally giving rise to the three germ layers. We compute the DM on an "ensemble-averaged" cell velocity dataset from 22 WT *Drosophila melanogaster* embryos undergoing gastrulation (33). Each velocity dataset was obtained combining in toto light sheet microscopy (11, 12) and tissue cartography (34) and consisted of coarse-grained velocities averaged with a spatial window of ≈5 cell size. The velocity field is given on 1,800 grid points over the fixed apical embryo surface (*SI Appendix*, Fig. S1) and covers a time interval of 40 min with a temporal resolution of 75 s, starting right after cephalic furrow (CF) formation. In *SI Appendix*, *Methods*, we provide the formulas for computing FTLE induced by cell motion on curved surfaces.

We computed the DM for a set of time scales $|T|$ spaced every 5 min. Fig. 4*A* shows the FW FTLE_0^{40} in the WT embryo. The diffuse high FTLE pattern on the lateral side marks the lateral region that will undergo high stretching during germ-band extension (GBE) (compare with cell trajectories in Movie S7). The D-pole repeller highlights a highly deforming area perpendicular to AP, and the P-pole repeller marks a second region of distinct high deformation during GBE. Fig. 4*E* shows the effect of the dorsal repeller on nearby cells. We performed a detailed analysis of the dorsal and posterior pole repellers in *SI Appendix*, Fig. S8 and show that FTLE provides an accurate time-scale-dependent map of Lagrangian deformations and cell repulsion. Movie S5 shows the FW FTLE field for different T.

Downloaded at Harvard Library on June 14, 2020

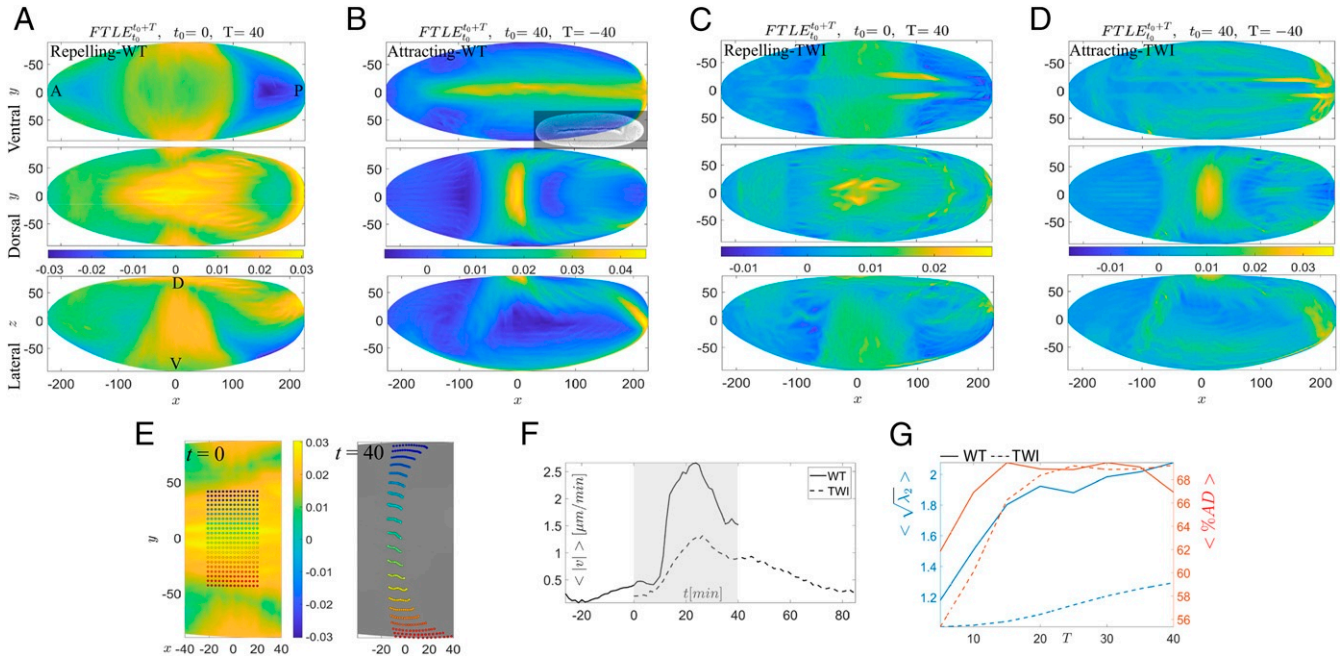


Fig. 4. (*A*) The FW $FTLE_0^{40}$ highlights two main repellers in the WT embryo. The FW FTLE evolution for different T is available as Movie S5. The FTLE has unit min^{-1}, and the axis units are in micrometers. (*B*) The BW $FTLE_{40}^{0}$ highlights the attracting LCSs in the WT embryo. *B*, *Inset* shows the VF from an embryo image obtained by LSM. The time evolution of BW FTLE for different T is available as Movie S6. Movie S7 is the same as Movie S6 along with the cells' position in green. (*C*) Same as *A* for an ensemble-averaged TWI mutant embryo. Movie S8 shows the FW FTLE for different T. (*D*) Same as *B* for an ensemble-averaged TWI mutant embryo. Movie S9 shows the BW FTLE for different T along with cell positions. (*E*) Effect of the ventral repeller in *A*, *Top* on nearby cells (see *SI Appendix*, Fig. S8*A* for a detailed analysis). (*F*) Spatially averaged speed of WT and TWI ensemble-averaged datasets. The gray area indicates the region of the analysis, and time 0 coincides with the first appearance of the cephalic furrow from LMS images. (*G*) Lagrangian tissue deformation quantified as the spatially averaged $\sqrt{\lambda_2}$ (blue). Red curves show the associated averaged anisotropic deformation contributions.

Movie S6 shows the BW FTLE field for different T whose last ($T = 40$) frame corresponds to Fig. 4*B*, and highlights three main attractors. The ventral furrow (VF) attractor forms around $t = 10$, the dorsal one around $t = 20$, and the U-shaped attractor close to the P pole at $t = 25$, which demarcates the posterior–lateral boundaries of the GBE. On the dorsal side, *Drosophila* gastrulation is characterized by several transverse structures, which include the already-formed CF, the anterior and posterior folds, and the posterior midgut invagination. Given the coarse-grained nature of the velocity field, structures whose width is smaller than five cell size cannot be fully resolved. The combined effect of the anterior and posterior folds, and the posterior midgut invagination, however, resulted in the strong transverse dorsal attractor that slightly moved from posterior to anterior, marking the dorsal boundary of the GBE. Movie S7 shows the BW FTLE along with cells' position, confirming the role of the attractors and repellers in shaping cell motion.

We performed the same analysis on an ensemble-averaged dataset from seven twist (TWI) mutant embryos (33). Time 0 min of WT and TWI datasets coincided with the first appearance of the CF from LMS images. Fig. 4*F* shows the spatially average speed of the two datasets, and the gray box indicates the time of our analysis when both WT and TWI velocities are available. Fig. 4 *C* and *D* show the same as Fig. 4 *A* and *B* for the TWI dataset. Twist embryos lack the VF attractor, as expected, and also show more diffused and weaker dorsal and posterior pole attractors compared to WT (compare *B* and *D*). The dorsal repeller is also significantly weaker and smaller than in the WT (compare *A* and *C*, *Middle*). Interestingly, the TWI embryo has two marked ventral repellers symmetric to the AP axis, which are not present in the WT. These repellers mark regions of cell separation induced by shear deformations, as shown in *SI Appendix*, Fig. S9. In Fig. 4*G*, we show that the overall tissue deformation, quantified as described above, is $\approx 60\%$ higher in the WT than in the TWI embryo within the first 40 min from CF formation, while the corresponding anisotropic deformation is the dominant contribution ($\geq 66\%$) in both. Although WT and TWI embryos genetically differ only locally in the ventral region where twist is expressed, such difference quickly induces global changes, which are promptly captured by the DM that shows marked differences also in the dorsal region. By contrast, the velocity field topology looks similar in WT and TWI datasets (Movie S10), except for the VF region during VF formation. We give a mathematical explanation of this difference in *SI Appendix*, *Methods C*. These results reaffirm that local morphogenetic changes can induce global effects, which are precisely quantified by our approach. Finally, comparing Movie S10 with Fig. 4 reinforces that the DMs reveal the key organizers of cell motion and quantify tissue deformations, both of which remain hidden to Eulerian velocity plots.

Conclusions

Using only available kinematic data associated with cell trajectories, we have provided a systematic kinematic framework for analyzing morphogenetic flows to uncover the evolving centerpieces of cell trajectory patterns, which we term the DM. The DM is frame invariant and based on a Lagrangian description of tissue deformation captured by the FTLE, which naturally combines local and global mechanisms along cell paths. The DM is composed of attracting and repelling LCSs toward which cells converge, or diverge from, over a specific time scale. Of particular note is evidence not just for attracting regions, but repelling regions that are just as important in determining cell fate. As

Downloaded at Harvard Library on June 14, 2020

aggregate measures, we have defined the overall Lagrangian tissue deformation and the corresponding isotropic and anisotropic fractions.

We have also shown that the DM provides information that is inaccessible to existing methods, such as the velocity field topology, simple inspection of cell trajectories, and deforming Lagrangian grids. In the cases we have studied, the DM either coincides with known morphogenetic structures and identifies their early footprints or reveals new ones which invariably shape trajectory patterns. In the chick PS formation, we have found that already within 1 h from freshly laid egg, the DM identifies the footprint of cells that will be part of the PS. Additionally, we have found a repeller that separates the AP cells within the PS and related it to gene expression patterns. Overall, comparing their DM and aggregate deformation measures, we have found that our approach quantitatively distinguishes WT and pathological embryos in both chick and fly morphogenesis.

Since the DM is driven solely by kinematic information, it is computable from cell-motion data and is agnostic to the mechanisms generating them. This is both an advantage and a disadvantage—as it provides a framework to study the organizers of development, and yet does not shed light on their origin. On the one hand, owing to its Lagrangian nature, we expect that the DM can help to quantify the relative importance of coexisting spatiotemporal mechanisms in morphogenesis. But to make it even more powerful, a natural next step is to connect the DM to known gene-expression patterns and mechanical processes, as well as identify new ones by performing targeted experiments to manipulate attractors and repellers.

Data Availability. The data and numerical codes are available to individual researchers on request from the corresponding author.

ACKNOWLEDGMENTS. We thank Antti Karjalainen and Ricardo Bango Da Cunha Correira for their contribution in generating the chicken embryo datasets; Matteo Rauzi, Adam Martin, and Yogesh Goyal for helpful discussions; and the anonymous reviewers for their insightful suggestions. M.S. was supported by the Schmidt Science Fellowship. M.C. and C.J.W. were supported by Biotechnology and Biological Sciences Research Council Grant BB/N009789/1. L.M. acknowledges support from NIH Grant 1R01HD097068, NIH Grant 1R01HD087234, and the NSF-Simons Center for Mathematical and Statistical Analysis of Biology at Harvard Grant 1764269.

1. K. Irvine, E. Wieschaus, Cell intercalation during *Drosophila* germband extension and its regulation by pair-rule segmentation genes. *Development* **120**, 827–841 (1994).
2. M. Leptin, *Drosophila* gastrulation: From pattern formation to morphogenesis. *Annu. Rev. Cell Dev. Biol.* **11**, 189–212 (1995).
3. J. Zallen, E. Wieschaus, Patterned gene expression directs bipolar planar polarity in *Drosophila*. *Dev. Cell* **6**, 343–355 (2004).
4. A. Martin, M. Kaschube, E. Wieschaus, Pulsed contractions of an actin–myosin network drive apical constriction. *Nature* **457**, 495–499 (2009).
5. G. Blanchard *et al.*, Tissue tectonics: Morphogenetic strain rates, cell shape change and intercalation. *Nat. Methods* **6**, 458–464 (2009).
6. L. C. Butler *et al.*, Cell shape changes indicate a role for extrinsic tensile forces in *Drosophila* germ-band extension. *Nat. Cell Biol.* **11**, 859–864 (2009).
7. C. Lye *et al.*, Mechanical coupling between endoderm invagination and axis extension in *Drosophila*. *PLoS Biol.* **13**, e1002292 (2015).
8. K. Irvine, B. Shraiman, Mechanical control of growth: Ideas, facts and challenges. *Development* **144**, 4238–4248 (2017).
9. P. J. Keller, Imaging morphogenesis: Technological advances and biological insights. *Science* **340**, 1234168 (2013).
10. P. J. Keller, A. D. Schmidt, J. Wittbrodt, E. H. Stelzer, Reconstruction of zebrafish early embryonic development by scanned light sheet microscopy. *Science* **322**, 1065–1069 (2008).
11. U. Krzic, S. Gunther, T. E. Saunders, S. J. Streichan, L. Hufnagel, Multiview light-sheet microscope for rapid in toto imaging. *Nat. Methods* **9**, 730–733 (2012).
12. R. Tomer, K. Khairy, F. Amat, P. J. Keller, Quantitative high-speed imaging of entire developing embryos with simultaneous multiview light-sheet microscopy. *Nat. Methods* **9**, 755–763 (2012).
13. F. Amat *et al.*, Fast, accurate reconstruction of cell lineages from large-scale fluorescence microscopy data. *Nat. Methods* **11**, 951–958 (2014).
14. C. Wolff *et al.*, Multi-view light-sheet imaging and tracking with the MaMuT software reveals the cell lineage of a direct developing arthropod limb. *eLife* **7**, e34410 (2018).
15. A. C. Oates, N. Gorfinkiel, M. Gonzalez-Gaitan, C. P. Heisenberg, Quantitative approaches in developmental biology. *Nat. Rev. Genet.* **10**, 517–530 (2009).
16. P. Gross, K. V. Kumar, S. W. Grill, How active mechanics and regulatory biochemistry combine to form patterns in development. *Annu. Rev. Biophys.* **46**, 337–356 (2017).
17. C. Truesdell, W. Noll, *The Non-Linear Field Theories of Mechanics* (Springer, Berlin, 2004).
18. L. Royer, W. Lemon, R. Chhetri, P. Keller, A practical guide to adaptive light-sheet microscopy. *Nat. Protoc.* **13**, 2462–2500 (2018).
19. K. McDole *et al.*, In toto imaging and reconstruction of post-implantation mouse development at the single-cell level. *Cell* **175**, 859–876 (2018).
20. F. Graner, B. Dollet, C. Raufaste, P. Marmottant, Discrete rearranging disordered patterns, part I: Robust statistical tools in two or three dimensions. *Eur. Phys. J. E Soft Matter* **25**, 349–369 (2008).
21. G. Haller, Lagrangian coherent structures. *Annu. Rev. Fluid Mech.* **47**, 137–162 (2015).
22. M. Serra, G. Haller, Objective Eulerian coherent structures. *Chaos* **26**, 053110 (2016).
23. A. Hadjighasem, M. Farazmand, D. Blazevski, G. Froyland, G. Haller, A critical comparison of Lagrangian methods for coherent structure detection. *Chaos* **27**, 053104 (2017).
24. E. Rozbicki *et al.*, Myosin-II-mediated cell shape changes and cell intercalation contribute to primitive streak formation. *Nat. Cell Biol.* **17**, 397–408 (2015).
25. H. Eyal-Giladi, S. Kochav, From cleavage to primitive streak formation: A complementary normal table and a new look at the first stages of the development of the chick: I. General morphology. *Dev. Biol.* **49**, 321–337 (1976).
26. V. Hamburger, H. L. Hamilton, A series of normal stages in the development of the chick embryo. *J. Morphol.* **88**, 49–92 (1951).
27. X. Yang, D. Dormann, A. E. Münsterberg, C. J. Weijer, Cell movement patterns during gastrulation in the chick are controlled by positive and negative chemotaxis mediated by FGF4 and FGF8. *Dev. Cell* **3**, 425–437 (2002).
28. Y. Hatada, C. D. Stern, A fate map of the epiblast of the early chick embryo. *Development* **120**, 2879–2889 (1994).
29. C. Alev *et al.*, Transcriptomic landscape of the primitive streak. *Development* **137**, 2863–2874 (2010).
30. M. Chuai *et al.*, Cell movement during chick primitive streak formation. *Dev. Biol.* **296**, 137–149 (2006).
31. K. M. Hardy, T. A. Yatskievych, J. Konieczka, A. S. Bobbs, P. B. Antin, FGF signalling through RAS/MAPK and PI3K pathways regulates cell movement and gene expression in the chicken primitive streak without affecting e-cadherin expression. *BMC Dev. Biol.* **11**, 20 (2011).
32. G. Zhao *et al.*, A novel, selective inhibitor of fibroblast growth factor receptors that shows a potent broad spectrum of antitumor activity in several tumor xenograft models. *Mol. Cancer Ther.* **10**, 2200–2210 (2011).
33. S. Streichan, M. Lefebvre, N. Noll, E. Wieschaus, B. Shraiman, Global morphogenetic flow is accurately predicted by the spatial distribution of myosin motors. *eLife* **7**, e27454 (2018).
34. I. Heemskerk, S. J. Streichan, Tissue cartography: Compressing bio-image data by dimensional reduction. *Nat. Methods* **12**, 1139–1142 (2015).

Downloaded at Harvard Library on June 14, 2020

PNAS
www.pnas.org

Supplementary Information for

Dynamic morphoskeletons in development

Mattia Serra, Sebastian Streichan, Manli Chuai, Cornelis J. Weijer and L. Mahadevan

Corresponding Author: L. Mahadevan
E-mail: lmahadev@g.harvard.edu

This PDF file includes:

Supplementary text
Figs. S1 to S9
References for SI reference citations

1. Supplementary Movies

MovieS1 Time evolution movie associated with Fig. 1b.
MovieS2 PIV velocity field of the wild-type chick embryo overlaid over the experimental fluorescence images of the epiblast surface.
MovieS3 Time evolution movie associated with Fig. 3a for different T. The lower panels show the averaged velocity field, the evolution of a dense set of points, and the deformation of an initially uniform grid that moves with the flow.
MovieS4 Time evolution movie associated with Fig. 3d for different T.
MovieS5 Time evolution movie associated with Fig. 4a for different T.
MovieS6 Time evolution movie associated with Fig. 4b for different T.
MovieS7 Time evolution movie associated with Fig. 4b for different T along with cell positions in green.
MovieS8 Time evolution movie associated with Fig. 4c for different T.
MovieS9 Time evolution movie associated with Fig. 4d for different T along with cell positions in green.
MovieS10 Velocity fields of WT and TWI mutant fly embryos.
MovieS11 Time evolution movie associated with Fig. S5 for different T.
MovieS12 Time evolution movie associated with Fig. S6 for different T.
MovieS13 Time evolution movie associated with Fig. S7 for different T.
MovieS14 Time evolution movie associated with Figs. S8a.
MovieS15 Time evolution movie associated with Figs. S8d.
MovieS16 Time evolution movie associated with Figs. S9.

Supporting Information Text

2. Methods

A. FTLE computation on a flat planar domain. We recall fom the main text (Eq. (2)), that the FTLE is defined as

$$FTLE^t_{t_0}(\mathbf{x}_0) = \frac{1}{|T|}\ln\left(\max_{\delta\mathbf{x}_0}\frac{|\overbrace{\nabla\mathbf{F}^t_{t_0}(\mathbf{x}_0)\delta\mathbf{x}_0}^{\delta\mathbf{x}_t}|}{|\delta\mathbf{x}_0|}\right) = \frac{1}{2|T|}\ln\left(\lambda_2(\mathbf{x}_0)\right), \quad \mathbf{C}^t_{t_0}(\mathbf{x}_0) = [\nabla\mathbf{F}^t_{t_0}(\mathbf{x}_0)]^\top\nabla\mathbf{F}^t_{t_0}(\mathbf{x}_0), \tag{1}$$

where $\lambda_2(\mathbf{x}_0)$ denotes the highest eigenvalue of the Cauchy–Green strain tensor $\mathbf{C}^t_{t_0}(\mathbf{x}_0)$, and $^\top$ matrix transposition. To compute the FTLE, we first calculate the flow map

$$\mathbf{F}^t_{t_0}(\mathbf{x}_0) = \mathbf{x}_0 + \int_{t_0}^{t}\mathbf{v}(\mathbf{F}^\tau_{t_0}(\mathbf{x}_0),\tau)\,d\tau, \tag{2}$$

which maps initial cell positions $\mathbf{x}_0$ at time t_0 to their time$-t$ position, by integrating the cell velocity field $\mathbf{v}(\mathbf{x},t)$ using the MATLAB built-in Runge-Kutta solver ODE45 with absolute and relative tolerance of 10^{-6}, linear interpolation in space and time, and a uniform grid of initial conditions $16\mu m$ apart from each other in both directions.

Then, denoting the $i-th$ component of the flow map $\mathbf{F}^t_{t_0}(\mathbf{x}_0)$ by $x^i(x^1_0,x^2_0,t_0,t)$, we compute the deformation gradient $\nabla\mathbf{F}^t_{t_0}(\mathbf{x}_0)$ using the finite-difference approximation (1)

$$\nabla\mathbf{F}^t_{t_0}(\mathbf{x}_0) \approx \begin{bmatrix} \frac{x^1(x^1_0+\delta,x^2_0,t_0,t)-x^1(x^1_0-\delta,x^2_0,t_0,t)}{2\delta} & \frac{x^1(x^1_0,x^2_0+\delta,t_0,t)-x^1(x^1_0,x^2_0-\delta,t_0,t)}{2\delta} \\ \frac{x^2(x^1_0+\delta,x^2_0,t_0,t)-x^2(x^1_0-\delta,x^2_0,t_0,t)}{2\delta} & \frac{x^2(x^1_0,x^2_0+\delta,t_0,t)-x^2(x^1_0,x^2_0-\delta,t_0,t)}{2\delta} \end{bmatrix}, \tag{3}$$

where $\delta = 16\mu m$ as the initial conditions' grid spacing. After computing $\nabla\mathbf{F}^t_{t_0}(\mathbf{x}_0)$, we use eq. Eq. (1) for computing the FTLE field.

B. FTLE computation on a curved surface. In the case of the Drosophila melanogaster dataset, the cell velocity field $\frac{d\mathbf{x}}{dt} = \mathbf{v}(\mathbf{x},t) = [u(\mathbf{x},t),v(\mathbf{x},t),w(\mathbf{x},t)]^\top \in \mathbb{R}^3$ is given on approximately 1800 points $\mathbf{x} = [x,y,z]^\top$ lying on the fixed apical embryo surface $\mathcal{S}\subset\mathbb{R}^3$, as illustrated in Fig. S1. We parametrize $\mathcal{S}$ in polar coordinates $\boldsymbol{\theta} = [\theta,\varphi]^\top \in \mathbb{S}^2$ as

$$\boldsymbol{\theta} = \mathbf{g}(\mathbf{x}) = \begin{bmatrix} \arctan\frac{y}{x} \\ \arcsin\frac{z}{\sqrt{x^2+y^2+z^2}} \end{bmatrix}, \quad \mathbf{x} = \mathbf{h}(\boldsymbol{\theta}) = \begin{bmatrix} \rho(\boldsymbol{\theta})\cos\varphi\cos\theta \\ \rho(\boldsymbol{\theta})\cos\varphi\sin\theta \\ \rho(\boldsymbol{\theta})\sin\varphi \end{bmatrix}, \tag{4}$$

where $\rho(\boldsymbol{\theta})$ is a cubic interpolant function that provides the distance of points on the embryo surface from the origin. The parametrization of any surface topologically equivalent to a two-dimensional sphere is known to possess singularities (cf. Eq. (4)). Indeed $\mathbf{g}$ is not defined at the dorsal (D) and ventral (V) poles. Therefore, we define a second parametrization, which has singularities at the anterior (A) and posterior (P) poles. Together, these two charts allow us to parametrize the embryo surface completely.

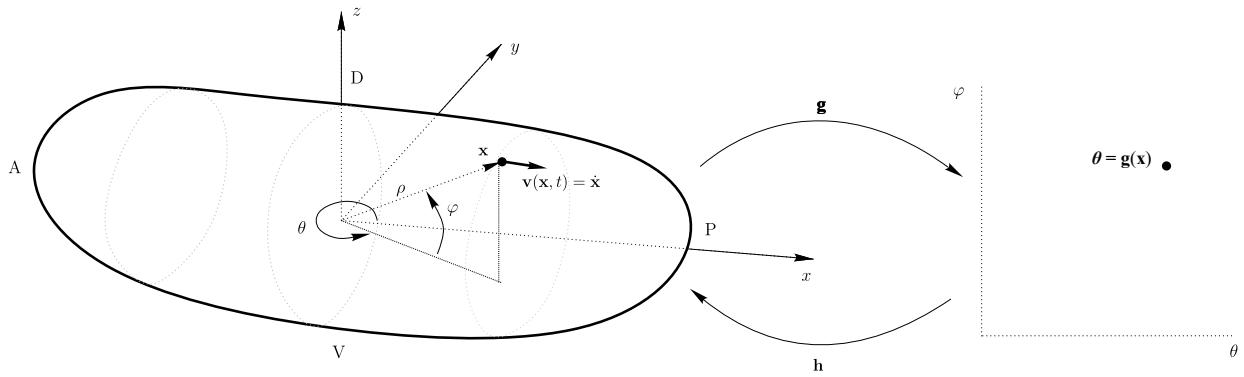


Fig. S1. Polar coordinates $\boldsymbol{\theta} = [\theta, \varphi]^\top \in \mathbb{S}^2$ parametrization of a Drosophila embryo apical surface given as a triangulated set of points $\mathbf{x} = [x, y, z]^\top \in \mathcal{S} \subset \mathbb{R}^3$. The points A,P,D and V mark the locations of the Anterior, Posterior, Dorsal and Ventral poles.

To compute cell trajectories, we have devised an in-house MATLAB code that integrates cell velocities over the triangulated surface using a Runge Kutta 4th order method. We ensure that trajectories remain on $\mathcal{S}$ by projecting current cell positions on $\mathcal{S}$ at each time step. We now define the Lagrangian flow map that maps an initial condition $\mathbf{x}_0$, parametrized by $\boldsymbol{\theta}$, to its final position as

$$\overbrace{\mathbf{F}_{t_0}^t(\mathbf{h}(\boldsymbol{\theta}))}^{\mathbf{x}_t} = \overbrace{\mathbf{h}(\boldsymbol{\theta})}^{\mathbf{x}_0} + \int_{t_0}^{t} \mathbf{v}(\mathbf{F}_{t_0}^{\tau}(\mathbf{h}(\boldsymbol{\theta})), \tau)\, d\tau. \tag{5}$$

From the Taylor expansion of the Lagrangian flow map with respect to $\boldsymbol{\theta}$, we obtain that

$$\overbrace{\mathbf{F}_{t_0}^t(\mathbf{h}(\boldsymbol{\theta}+\boldsymbol{\delta\theta})) - \mathbf{F}_{t_0}^t(\mathbf{h}(\boldsymbol{\theta}))}^{\delta\mathbf{x}_t} \approx \nabla_{\boldsymbol{\theta}}[\mathbf{F}_{t_0}^t(\mathbf{h}(\boldsymbol{\theta}))]\delta\boldsymbol{\theta}. \tag{6}$$

Using Eqs. (1,6), we rewrite the FTLE in the case of motion on curved surfaces as

$$\begin{aligned} FTLE_{t_0}^t(\boldsymbol{\theta}) =& \frac{1}{|T|} \ln\left(\max_{\delta\boldsymbol{\theta}} \frac{|\nabla_{\boldsymbol{\theta}}[\mathbf{F}_{t_0}^t(\mathbf{h}(\boldsymbol{\theta}))]\delta\boldsymbol{\theta}|}{|\nabla_{\boldsymbol{\theta}}\mathbf{h}(\boldsymbol{\theta})\delta\boldsymbol{\theta}|} \right) \\ =& \frac{1}{|T|} \ln\left(\max_{\delta\boldsymbol{\theta}} \sqrt{\frac{\langle \delta\boldsymbol{\theta}, (\nabla_{\boldsymbol{\theta}}[\mathbf{F}_{t_0}^t(\mathbf{h}(\boldsymbol{\theta}))])^\top (\nabla_{\boldsymbol{\theta}}[\mathbf{F}_{t_0}^t(\mathbf{h}(\boldsymbol{\theta}))])\delta\boldsymbol{\theta}\rangle}{\langle \delta\boldsymbol{\theta}, [\nabla_{\boldsymbol{\theta}}\mathbf{h}(\boldsymbol{\theta})]^\top [\nabla_{\boldsymbol{\theta}}\mathbf{h}(\boldsymbol{\theta})]\delta\boldsymbol{\theta}\rangle}} \right), \end{aligned} \tag{7}$$

where $\langle , \rangle$ denotes the dot product. Using the relations in Eq. (5), we note that $\nabla_{\boldsymbol{\theta}}[\mathbf{F}_{t_0}^t(\mathbf{h}(\boldsymbol{\theta}))]$ is simply the Jacobian of the 3D Flow map, whose $i-th$ component is $x^i(\varphi, \theta, t_0, t)$, with respect to $\boldsymbol{\theta} = [\varphi, \theta]$, and hence can be computed by finite differencing as described in Eq. (3). Similarly, $[\nabla_{\boldsymbol{\theta}}\mathbf{h}(\boldsymbol{\theta})]$ is the Jacobian of the 3D Flow map evaluated at $t = t_0$ with respect to $\boldsymbol{\theta}$, and can be computed either as in Eq. (3) or by explicitly using the form of the parametrization in Eq. (4) as

$$\nabla_{\boldsymbol{\theta}}\mathbf{h}(\boldsymbol{\theta}) = \begin{bmatrix} \partial_\theta\rho(\boldsymbol{\theta})\cos\varphi\cos\theta - \rho(\boldsymbol{\theta})\cos\varphi\sin\theta & \partial_\varphi\rho(\boldsymbol{\theta})\cos\varphi\cos\theta - \rho(\boldsymbol{\theta})\sin\varphi\cos\theta \\ \partial_\theta\rho(\boldsymbol{\theta})\cos\varphi\sin\theta + \rho(\boldsymbol{\theta})\cos\varphi\cos\theta & \partial_\varphi\rho(\boldsymbol{\theta})\cos\varphi\sin\theta - \rho(\boldsymbol{\theta})\sin\varphi\sin\theta \\ \partial_\theta\rho(\boldsymbol{\theta})\sin\varphi & \partial_\varphi\rho(\boldsymbol{\theta})\sin\varphi + \rho(\boldsymbol{\theta})\cos\varphi \end{bmatrix}, \tag{8}$$

where $\partial_\varphi\rho(\boldsymbol{\theta}), \partial_\theta\rho(\boldsymbol{\theta})$ need to be computed by finite differencing. The symmetric tensor $\mathbf{G}(\boldsymbol{\theta}) = [\nabla_{\boldsymbol{\theta}}\mathbf{h}(\boldsymbol{\theta})]^\top [\nabla_{\boldsymbol{\theta}}\mathbf{h}(\boldsymbol{\theta})]$ is the metric tensor of the embryo surface at point $\mathbf{h}(\boldsymbol{\theta})$. We illustrate Eqs. (5-7) in Fig. S2.

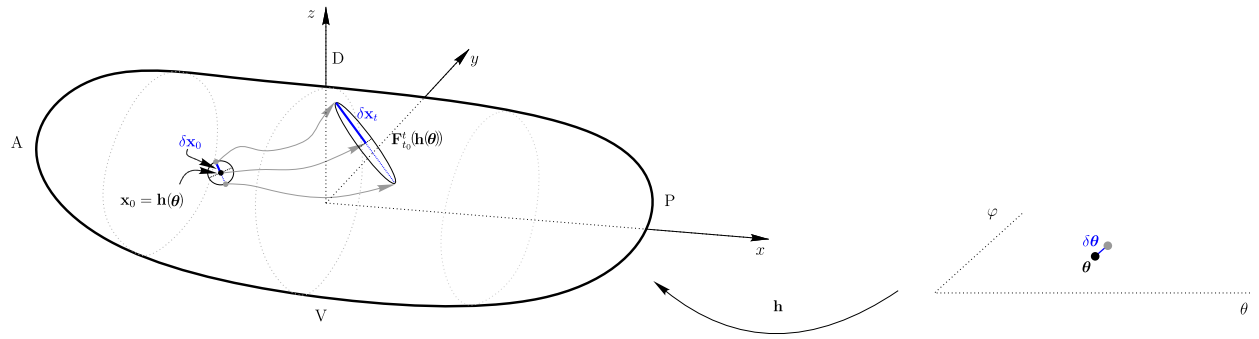


Fig. S2. Time evolution of the relative position vector $\delta\mathbf{x}_t$ between two initially close cells on the embryo surface as a function of polar coordinates (cf. Eqs. (5-6)).

In our analysis, we define a uniform grid of initial conditions $\boldsymbol{\theta}$ spaced by 1 $deg.$, compute 3D trajectories as described above, and the Jacobian matrices in Eq. (7) using finite differencing with step size $\delta = 1deg.$. Finally, we parameterize $\delta\boldsymbol{\theta} = [\cos\alpha, \sin\alpha]^\top$ and compute Eq. (7) numerically using a vector of possible α from 0 to 2π spaced by $1deg.$.

C. Eulerian and Lagrangian assessment of tissue deformations. We recall a known relation (see e.g. (2) for derivation) between the Eulerian rate of strain tensor, broadly used for studying deformations in morphogenesis, and the Lagrangian Cauchy-Green tensor.

$$\sqrt{\frac{\langle \delta\mathbf{x}_0, \mathbf{C}_{t_0}^t(\mathbf{x}_0)\delta\mathbf{x}_0\rangle}{\langle \delta\mathbf{x}_0, \delta\mathbf{x}_0\rangle}} = \frac{|\delta\mathbf{x}_t|}{|\delta\mathbf{x}_0|} = \mathrm{Exp}\left[\int_{t_0}^{t} \frac{\langle \nabla\mathbf{F}_{t_0}^\tau(\mathbf{x}_0)\delta\mathbf{x}_0, \mathbf{S}(\mathbf{F}_{t_0}^\tau(\mathbf{x}_0),\tau)\nabla\mathbf{F}_{t_0}^\tau(\mathbf{x}_0)\delta\mathbf{x}_0\rangle}{\langle \nabla\mathbf{F}_{t_0}^\tau(\mathbf{x}_0)\delta\mathbf{x}_0, \nabla\mathbf{F}_{t_0}^\tau(\mathbf{x}_0)\delta\mathbf{x}_0\rangle} d\tau\right] \quad [9]$$

To gain a better intuition of the differences between an Eulerian assessment of deformation encoded in $\mathbf{S}$, and the corresponding Lagrangian (i.e. with memory) one, we consider two velocity fields one multiple of each other $\tilde{\mathbf{v}}(\mathbf{x},t) = c\mathbf{v}(\mathbf{x},t)$. The corresponding rate of strain tensors are related by $\tilde{\mathbf{S}}(\mathbf{x},t) = c\mathbf{S}(\mathbf{x},t)$, hence having the same eigenvectors and topology of the eigenvalues. By contrast, the Lagrangian deformation encoded in $\mathbf{C}_{t_0}^t(\mathbf{x}_0)$ will have different spatial structures for a fix $[t_0, t]$ in these two systems because cell paths in the modified flow $\tilde{\mathbf{F}}_{t_0}^t(\mathbf{x}_0) = \mathbf{x}_0 + c\int_{t_0}^t \mathbf{v}(\tilde{\mathbf{F}}_{t_0}^\tau(\mathbf{x}_0),\tau)\, d\tau$ will visit different points compared to the original one (Eq. (2)). A similar reason holds for the associated deformation gradient $\tilde{\nabla}\tilde{\mathbf{F}}_{t_0}^t(\mathbf{x}_0) = \mathbf{I} + c\int_{t_0}^t \nabla\mathbf{v}(\tilde{\mathbf{F}}_{t_0}^\tau(\mathbf{x}_0),\tau)\tilde{\nabla}\tilde{\mathbf{F}}_{t_0}^\tau(\mathbf{x}_0)\, d\tau$. These simple relations highlight that both uniform as well as localized changes of tissue flows can lead to global changes, which can be detected by Lagrangian methods while remaining inaccessible to Eulerian ones.

D. Isotropic and anisotropic contribution to Lagrangian attraction. We recall that attracting LCSs, captured by the backward FTLE, can occur because of isotropic contraction or anisotropic deformation, as described in the main text. We denote by $|\delta\mathbf{x}_t^\top| = |\delta\mathbf{x}_0| + \Delta^I + \Delta^A$ the final distance of two particles initially distant $|\delta\mathbf{x}_0|$, where Δ^I, Δ^A denote the distance change due to isotropic and anisotropic deformations. The isotropic area shrinkage induced by $\mathbf{F}_{t_0}^t(\mathbf{x}_0)$ on an infinitesimal patch centered at $\mathbf{x}_0$ can be computed as

$$\frac{A_t(\mathbf{x}_0)}{A_0(\mathbf{x}_0)} = \sqrt{\det \mathbf{C}_{t_0}^t(\mathbf{x}_0)}, \quad t < t_0, \quad [10]$$

and induces particle convergence in forward time, as illustrated and quantified in Fig. S3 (Center). This scalar field is based at the final configuration $\mathbf{x}_0$ and integrates information over the time interval $[t, t_0]$. It attains values greater than unity in regions where initially far trajectories converge because of isotropic contraction, and is less than unity in regions where initially close trajectories diverge due to isotropic expansion. We compute the convergence due to anisotropic deformation as the total convergence minus the one from isotropic shrinkage (Fig. S3 Right). Using the expressions in Fig. S3, we define the percentage

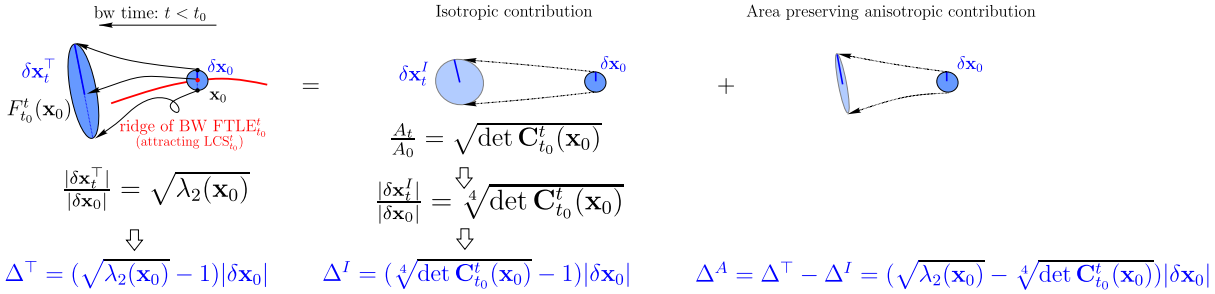


Fig. S3. (Left) Backward FTLE ridge as in Fig. 2b. The BW FTLE is a rescaled form of the maximum convergence achieved by two initially distant particles in forward time. (Center) Particles convergence induced by isotropic area contraction quantified by eq. Eq. (10). (Right) Particles convergence due to area preserving anisotropic deformation.

of Lagrangian attraction due to anisotropic deformation as

$$\%An.Def._{t_0}^t(\mathbf{x}_0) = \frac{\Delta^A}{|\Delta^I| + \Delta^A}\% = \left(\frac{\sqrt{\lambda_2(\mathbf{x}_0)} - \sqrt[4]{\det \mathbf{C}_{t_0}^t(\mathbf{x}_0)}}{|\sqrt[4]{\det \mathbf{C}_{t_0}^t(\mathbf{x}_0)} - 1| + \sqrt{\lambda_2(\mathbf{x}_0)} - \sqrt[4]{\det \mathbf{C}_{t_0}^t(\mathbf{x}_0)}}\right) 100, \quad t < t_0, \quad [11]$$

which completely characterize the Lagrangian cell convergence. Because $\det \mathbf{C}_{t_0}^t(\mathbf{x}_0) = \lambda_1(\mathbf{x}_0)\lambda_2(\mathbf{x}_0)$ and $\lambda_1(\mathbf{x}_0) \leq \lambda_2(\mathbf{x}_0)$ by definition, it follows that $\Delta^A \geq 0$. Note that if the cell velocity field is incompressible ($\nabla\cdot\mathbf{v} = 0$), by Liouville's formula (3) $\det \mathbf{C}_{t_0}^t(\mathbf{x}_0) = 1$, and $\%An.Def._{t_0}^t(\mathbf{x}_0) = 100$ as all the attraction is caused by anisotropic deformations. Conversely, if anisotropic deformations are absent, an initially circular patch remains circular, hence the two eigenvalues of $\mathbf{C}_{t_0}^t(\mathbf{x}_0)$ characterizing the deformed ellipse semi axes are identical $\lambda_2(\mathbf{x}_0) = \lambda_1(\mathbf{x}_0) = \lambda(\mathbf{x}_0)$. Therefore, it follows that $\sqrt[4]{\det \mathbf{C}_{t_0}^t(\mathbf{x}_0)} = \sqrt[4]{\lambda_2(\mathbf{x}_0)\lambda_1(\mathbf{x}_0)} = \sqrt[4]{\lambda^2(\mathbf{x}_0)} = \sqrt{\lambda(\mathbf{x}_0)}$, which makes $\%An.Def._{t_0}^t(\mathbf{x}_0) = 0$, as desired.

3. Chordin and Wnt8C expression patterns during primitive streak formation in chicken embryo

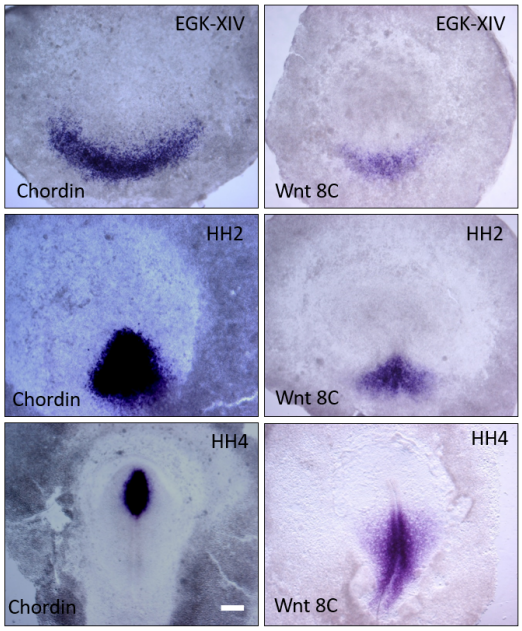


Fig. S4. Chordin and Wnt8C expression patterns in pre and gastrulation stage chick embryos. Embryos were fixed at different stages (EGK-XIII, HH2 and HH4) of development and RNA expression detected using standard in-situ hybridisation procedures (4). Both Chordin and Wnt8c are initially expressed in a sickle shape region in the posterior chick epiblast, followed by their separation during streak extension. Chordin is expressed in the anterior streak, while Wnt8c is expressed in the posterior streak and the mesoderm cells that migrate from out of the posterior streak. White scale bar 0.5mm.

4. Lagrangian deformation types behind primitive streak formation in chicken embryo

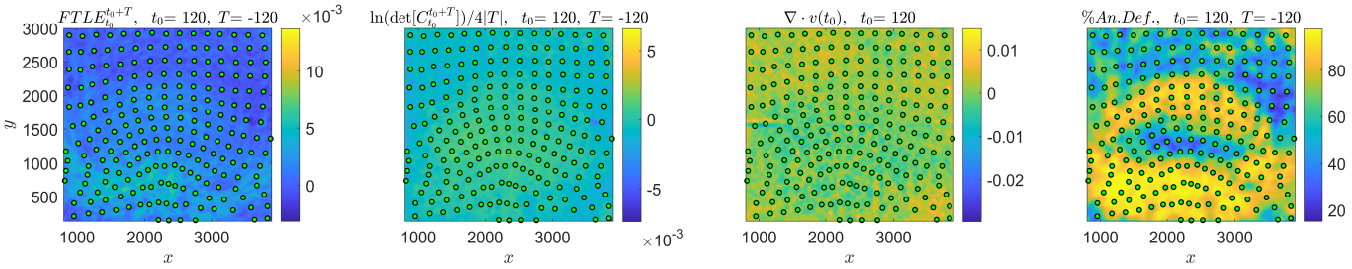


Fig. S5. (First) BW FTLE of the wild-type chick embryo corresponding to $|T| = 2h$ shortly after egg laying (stage EKG XII), whose high values demarcates the forming PS. (Second) Isotropic Lagrangian attraction field (quantified Fig. S3 Center) rescaled by the logarithm and normalized by $|T|$, as in the FTLE definition. (Third) Eulerian velocity field divergence. The first three scalar fields are in min^{-1}. (Fourth) $\%An.Def._{t_0}^{t}(\mathbf{x}_0)$ field defined in Eq. (11). Movie S11 shows the full evolution of the above scalar fields for different T, along with cells position (green).

The first panel of Fig. S5 shows the BW FTLE and cell positions corresponding to $|T| = 2h$ for the chick wild-type embryo analyzed in Fig. 3(a). The second panel shows the Lagrangian Isotropic attraction rescaled by the logarithm and normalized by $|T|$, as in the FTLE definition. The high BWFTLE value region, capturing the forming PS, is completely hidden in the Isotropic attraction field, which attains higher values in the middle of the domain. The forming PS is also completely hidden to the velocity divergence field (third panel), which is the instantaneous version ($T \to 0$) of the Lagrangian area shrinkage in the second panel, and whose negative values demarcate regions characterized by instantaneous isotropic contraction. The right panel shows the $\%An.Def.$ field defined in eq. Eq. (11) highlighting that the high BW FTLE region in the First panel is mainly ($\geq 80\%$) due to anisotropic deformation. Movie S11 shows the time evolution of Fig. S5 for different T, and indicates that cell convergence giving rise to the PS is always dominated by anisotropic tissue deformation.

5. Morphogenetic features extraction from the FTLE field

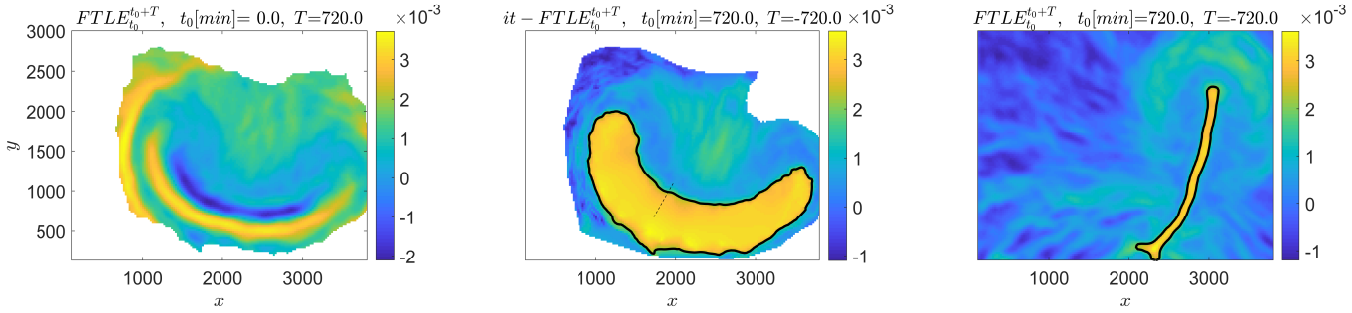


Fig. S6. Same scalar fields as in Fig. 3(a) smoothed with an average filter of window size 3x3. (Left) FW FTLE field. (Center) BWFTLE passively transported at the initial time. The solid black line is a level set of the BWFTLE field delimiting the area of cells that will form the PS at their initial positions. The level set value is automatically selected evaluating the BWFTLE along the dashed black segment (from bottom to top) and detecting the value at which the derivative is minimal. (Right) BWFTLE based at the final time. The solid black curve is the BWFTLE level set corresponding to the value identified in the center panel. Movie S12 shows the full evolution of the above scalar fields for different T. We compute the area enclosed by the black solid line in the center panel by using an in-built MATLAB function.

6. Dynamic Morphoskeletons behind primitive streak formation in chicken embryo using unfiltered velocity data

While filtering velocities is necessary for Eulerian methods, owing to their sensitivity to noise and measurement errors, it may hide finer-scale structures whose characteristic sizes are smaller than the filtering window sizes. By contrast, Lagrangian methods are intrinsically more robust because the integration of cell velocities along trajectories acts like a filter.

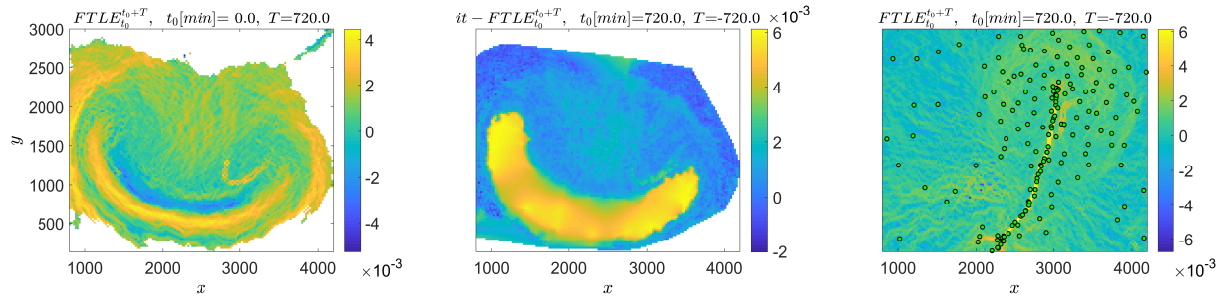


Fig. S7. Same scalar fields as in Fig 3a, computed from raw (unfiltered) velocity data. (Left) FW FTLE corresponding to the full extent of the dataset ($|T| = 12h$ from the freshly laid egg stage), whose high values demarcates two repelling LCSs as described in in Fig 3a. (Right) BW FTLE corresponding to the full extent of the dataset whose strong ridge highlights the attracting LCS corresponding to the formed PS. Cells position at $12h$, initialized from a uniform gird at $0h$, are shown by green dots. White areas correspond to regions where the FTLE is unavailable because trajectories left the domain over which the velocity field is defined. (Center) BW FTLE shown in (Right) passively transported by F_{720}^{0} shows the initial cell positions that will finally form the PS. The FTLE has unit $\mathrm{min}^{-}1$, the axis units are in μm and the posterior anterior direction goes from smaller to larger y values. Movie S13 shows the full time evolution of BW and FW FTLE for different T, along with cells position.

7. Drosophila Melanogaster WT: dorsal and posterior pole repellers

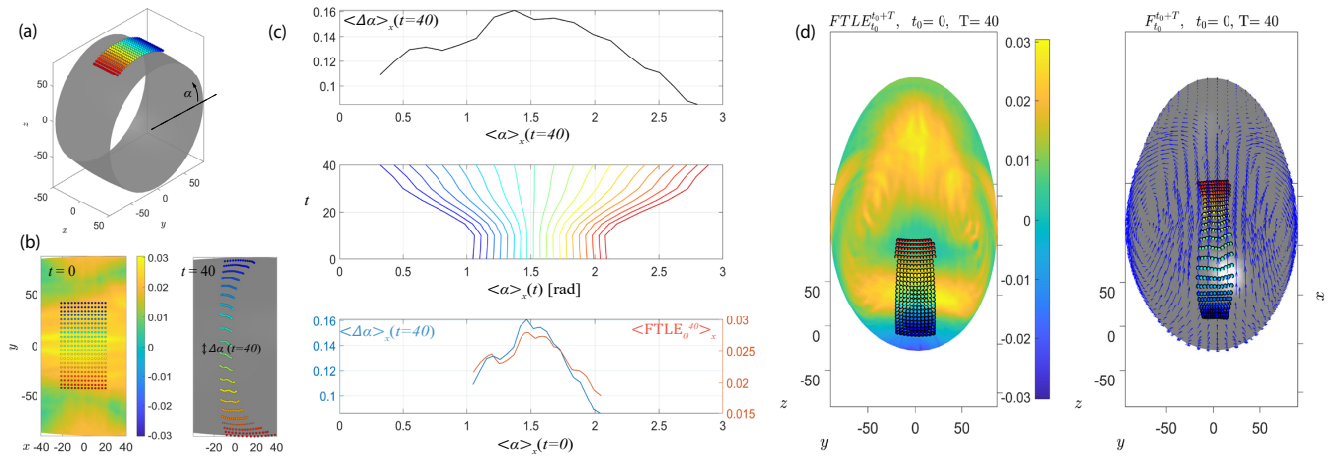


Fig. S8. (a-c) Dorsal repeller in the WT drosophila dataset illustrated in Figs. 4a,e. (a) Initial cell positions placed across the dorsal repeller color-coded by increasing values of α. (b) Left: dorsal view of the initial cell positions shown in (a) along with the corresponding FTLE_0^{40} field encoded in the colorbar. Right: final cell positions. Movie S14 shows cell positions over time. (c) Center: Kymograph of $x-$averaged angular position $< \alpha >_x (t)$ for the color-coded rows of points shown in (a,b). Top: $x-$averaged angular distance $< \Delta\alpha >_x (t = 40)$ between consecutive rows of points (see panel b) graphed over $< \alpha >_x (t = 40)$. Bottom: $x-$averaged angular distance (blue) between consecutive rows of points graphed over $< \alpha >_x (t = 0)$. The red curve shows the $x-$averaged FTLE_0^{40} in correspondence of the initial grid of cells (panel b) for different values of α. (d) Same analysis of (b) for the posterior pole repeller in the WT drosophila dataset shown in Fig. 4a along with cell velocity field in blue. Movie S15 shows the time evolution of cell positions and velocities. The FTLE has unit $\min^- 1$, and the Cartesian axis units are in μm.

Figures S8a-c illustrate the influence of the dorsal repeller in the WT drosophila dataset (cf. Figs. 4a,e). We place a set of cells across the dorsal repeller color-coded by increasing values of α (a). We show the initial and final cell positions in (b) along with a movie with intermediate time steps (Movie S14). The scalar field in the left panel encodes FTLE_0^{40}. Using a kymograph, we plot the tissue deformation across the repeller in (c) center. For each color-coded row of points, we compute the $x-$averaged angular position $< \alpha >_x (t)$. In the top panel, we show the $x-$averaged angular distance $< \Delta\alpha >_x (t = 40)$ between consecutive rows of points (see panel b) graphed over $< \alpha >_x (t = 40)$. We graph the same quantity in the bottom panel over $< \alpha >_x (t = 0)$ (blue curve) along with the $x-$averaged FTLE_0^{40} (red curve) in correspondence of the initial grid of cells (panel b) for different values of α. Although the FTLE ridge is diffuse, peaks of $< \text{FTLE}_0^{40} >_x$ accurately predict embryo regions that will undergo the highest stretching.

To check tissue deformations from the FTLE, we note that for $\alpha \approx \pi/2$, $< \text{FTLE}_0^{40} >_x \approx 0.027$, which implies a stretching $\sqrt{\lambda_2} \approx 2.9$. For the rows of points starting at $\alpha \approx \pi/2$, $< \Delta\alpha >_x (t = 40) \approx 0.15$. Assuming only deformation along α, from the relative displacement of cells $\sqrt{\lambda_2} \approx \frac{R\Delta\alpha(t=40)}{R\Delta\alpha(t=0)} = \frac{0.15}{3\pi/180} \approx 2.9$, where we used that $R \approx 50\mu m$ (panel a) remains constant between initial and final cell positions, and that the initial α spacing of cell rows is 3 $deg.$. This confirms that the FWFTLE marks regions of distinct repulsion as well as quantifies areas of maximum tissue deformation over a desired T. This characterization, by contrast, remains hidden to Eulerian methods and cell trajectory plots.

Figure S8b shows the same analysis of panel (b) for the posterior pole repeller in the WT drosophila dataset shown in Fig. 4a along with the cell velocity field in blue. During GBE, the repeller highlights the precise region of distinct cell separation (and tissue deformation), which is confirmed by the relative motion of color-coded cells. Specifically, the color-coded rows of cells that start within the repeller undergo visibly higher separation compared to the nearby rows. Movie S15 shows the corresponding time evolution of cell positions, further illustrating that the Lagrangian repeller is inaccessible to Eulerian velocity plots.

8. Drosophila Melanogaster TWI: ventral repellers

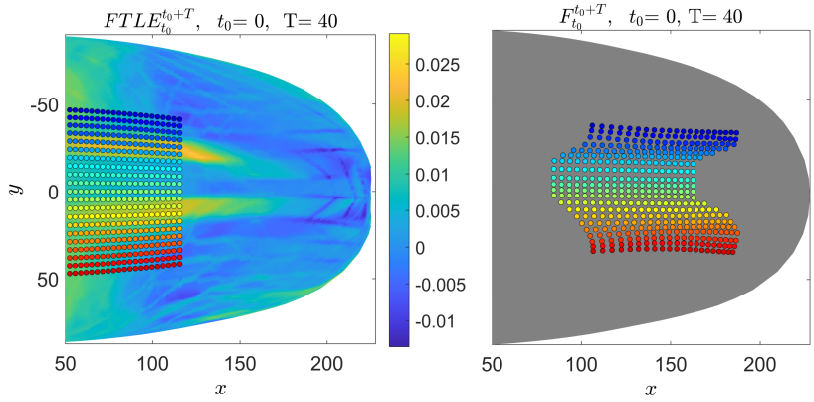


Fig. S9. Left: FWFTLE$_0^{40}$ shows two ventral repellers in the TWI drosophila dataset. Dots indicate initial cell positions color-coded for increasing values of α, as in Fig. S8a. Right: final cell positions confirm that cells across the repellers undergo high separation induced by shear deformations. Movie S16 shows cell positions over time. The FTLE has unit $\mathrm{min}^{-}1$, and the Cartesian axis units are in μm.

References

1. Haller G (2001) Distinguished material surfaces and coherent structures in three-dimensional fluid flows. *Physica D* 149(4):248–277.
2. Serra M, Vétel J, Haller G (2018) Exact theory of material spike formation in flow separation. *J. Fluid Mech.* 845:51–92.
3. Guckenheimer J, Holmes P (1983) *Nonlinear oscillations, dynamical systems, and bifurcations of vector fields*. (Springer Science & Business Media) Vol. 42.
4. Wilkinson DG, Nieto MA (1993) [22] detection of messenger rna by in situ hybridization to tissue sections and whole mounts in *Methods in enzymology*. (Elsevier) Vol. 225, pp. 361–373.